Electronic Supplementary Material (ESI) for Inorganic Chemistry Frontiers.

Regulation of Polyaniline Thickness and Substitution Position on Cu Foam to Optimize Hydrogen Evolution and Ethanol Oxidation Performance

Haiqiang Mu[a], Pengyue Shan[b], Min Zhu[a], Zhenli Lv[a], Guorui Ma[a], Jiaxing Guo[a], Junzhuo Fang[c], Jin Zhang[c], Feng Li[a]*, Jing Li[a]*

[a.] College of Chemistry and Chemical Engineering, Ningxia University, Yinchuan, Ningxia, 750021, P. R. China.

[b.] Key Laboratory of Energy Thermal Conversion and Control of Ministry of Education, School of Energy and Environment, Southeast University, Nanjing 210096, China.

[c.] Analysis and Testing Center, Ningxia University, Yinchuan, Ningxia, 750021, P. R. China.

* Corresponding author.

E-*mail address:* jingli18@nxu.edu.cn (Jing Li), fengli@nxu.edu.cn (Feng Li).

2. Experimental section

2.1 Material

Acetonitrile, tetrabutylammonium hexafluorophosphate, Iodobenzene (C_6H_5I, 99%), o-iodonitrobenzene ($C_6H_4INO_2$, 99%), p-iodonitrobenzene ($C_6H_4INO_2$, 98%), m-iodonitrobenzene ($C_6H_4INO_2$, 98%) were purchased from Aladdin Reagent Co., Ltd. Argon (Ar) with the purity of 99.995%, Cu foam (with the purity of 99.99% and the thickness of 0.3 mm) were used. All deionized water used in the experiment was purified by a Milli Q water purification system (18.2 mΩ cm^{-1}); and all chemicals were used without further purification.

2.2 Materials Synthesis.

2.2.1 Synthesis of polymer-modified Cu foam electrode.

The different polymer-modified Cu foam electrode was prepared by electrografting method. In general, the electrode of Cu foam (20×10×0.3 mm) was respectively cleaned in deionized water, 0.1 M HCl solution, and acetone to remove any impurities and oxide layers on it. Then, the electrode was rinsed with water and dried up under Ar. Electrografting was performed by a cyclic voltammetry (CV) method in a single compartment cell using a three-electrode system: unmodified Cu foam (bare-Cu foam) as a working electrode, a platinum plate as a counter electrode, and Ag/AgCl (saturated KCl) as a reference electrode. Before electrografting, Ar was passed through the organic solution for about 30 minutes to remove O_2. The CV was performed in

acetonitrile solution of p-iodonitrobenzene (6 mM) and tetrabutylammonium hexafluorophosphate (0.15 M) with a scan rate of 100 mV s^{-1} between -0.8 and -3.2 V vs. Ag/AgCl, in which CV cycle numbers were set to 210. After modification, Cu/PANI-210 was washed by ultrasonication in acetonitrile and ultrapure water for 5 min each.

In general, the action of synthesizing BP/CF-210, m-PANI/CF-210 and o-PANI/CF-210 followed the same procedure as above, except that organic matter "p-iodonitrobenzene" were changed to "Iodobenzene, m-iodonitrobenzene and o-iodonitrobenzene".

2.2.2 Synthesis of aniline-modified Cu foam electrode.

After cleaning and drying, the CF was soaked in aniline (ANI) for 72 hours to obtain ANI/CF.

2.3 Characterization

The cold field emission scanning electron microscope (F-SEM) (TY2020003841 Regulus8100) images were taken to identify the morphologies of the samples. Transmission electron microscopy (TEM, acceleration voltage: 200 kV) was performed on FEI Tecnai G2 20 microscope (FEI, Hillsboro, OR, USA) linked to an X-ray energy dispersive spectrometer (EDS). The X-ray diffraction (XRD) measurements of samples were performed on D8 ADVANCE A2503040614, ≥ 3 kW to determine its crystal structure. The synthesis of PANI/CF-210 and ANI/CF were analyzed with FT-IR

analysis (FT-IR S2, Spectrum Two, USA). Samples were prepared in discs forms using spectroscopic grade KBr powder. Moreover, an INVENIO-R (Bruker) Fourier transform infrared (FTIR) spectrometer equipped with a mercury cadmium telluride (MCT-A) detector cooled with liquid nitrogen was employed for the operando spectroelectrochemical FTIR studies. The XPS spectra of samples were collected on the PerkinElmer PHI-5702 using Al-Kα radiation. All data were corrected using the C 1s peak at 284.8 eV as an internal standard. Raman spectroscopy measurements were performed on a DXR 2xi Raman microscope imaging spectrometer with an excitation laser of 532 nm (Thermo Fisher Scientific, Waltham, UK). Bruker AVANCE III 400 MHz nuclear magnetic resonance (NMR) spectrometer was used to investigate the liquid products. The gaseous products were tested by a gas chromatography (GC-8860, Agilent). The contained thermal conductivity detector (FID) connected to a Porapak Q packed column (Agilent Technologies, Inc.) to detect H_2 and O_2. The N_2 adsorption-desorption isotherms were measured by a TriStar 3000 volumetric adsorption analyzer at liquid nitrogen temperature. Each sample was sufficiently heated in a vacuum at 150 °C for 8 h before measurement

2.4 Electrochemical measurements

The performance curves concerning HER, OER and EOR were recorded with a CHI 760E electrochemical workstation (CH Instruments, China). The platinum plate, Ag/AgCl (saturated KCl) and CF modified with different polymer compounds was respectively used as the counter electrode, reference electrode and working electrode.

During the test, after sufficient activation and stabilization in cyclic voltammetry (CV) mode, linear sweep voltammetry (LSV) curves were collected by a sweep step width of 5 mV s^{-1} to assess the HER performance of the catalyst. The Tafel slope was determined using LSV curves fitted with the equation: $\eta = a + b (\log |j|)$. Electrochemical impedance spectroscopy (EIS) was measured at a selected voltage using a frequency range of 0.1 Hz ~ 100 kHz (amplitude of 5 mV), where the intercept and radius on the horizontal axis represented the values of solution resistance (R_s) and charge transfer resistance (R_{ct}), respectively. Specifically, CV were collected at different scan rates in a narrow potential window where no Faraday reaction occurred. Electrochemical active surface area (ECSA) was attained by calculating the corresponding C_{dl} ratio relative to the copper foam substrate. For the study of stability, the CV cycling test was carried out for 1000 cycles over a voltage range of 0.3 V at a scan rate of 50 mV s^{-1}. The LSV curves before and after the tests were collected at a scan rate of 5 mV s^{-1}. Besides, the chronopotentiometry test operated continuously for about 30 h at an applied voltage in 0.5 M H_2SO_4 solution. The liquid phase EOR products were identified by ^1H NMR (400 MHz, Bruker AV III 40003140403). DMSO serves as an internal standard. All the experimental data were calibrated with respect to reversible hydrogen electrode (RHE) by $E_{RHE} = E_{Ag/AgCl} + 0.0591\ (pH) + 0.241$ V.

2.5 Electrochemical *In Situ* FTIR Spectra Measurements

the measurement of electrochemical in situ Fourier transform infrared (in situ FTIR) reflection spectroscopy was conducted on a INVENIO-R (Bruker) spectrometer

containing a liquid-nitrogen-cooled MCT-A detector. The species produced by PANI/CF-210 during EOR were measured on the working electrode and in situ FTIR CaF_2 substrate. And multi-stepped FTIR spectroscopy (MS-FTIR) was utilized to collect spectra in 1.0 M KOH electrolyte with 1.0 M ethanol electrolyte from 0.8 to 1.6 V vs. RHE) at 0.1 V intervals. The resolution for the real-time FTIR reflection absorption spectroscopy spectra is 8 cm^{-1} with 32 scans per spectrum.

2.6 Studies of the Existence State of H^+ on the Surface of Electrocatalyst.

The following method determines how much H^+ is collected by PANI: The C_6H_5NH monounits that make up the PANI have an H^+-capturing site at the $-NH_2$. One H^+ is captured by each C_6H_5NH monounit. A 4 mL solution of 0.001 M ($pH = 11$) NaOH was used as the H^+ neutralizer in this investigation. The sample with a 2 cm^2 geometric surface area was used, and the pH value of the NaOH solution after neutralization was measured using a pH detector (PHS-4CT, Shanghai, China). The amount of H^+ captured by PANI (per cm^2) can be calculated via

$$n(H^+)\ (mol/cm^2) = [0.001 - 10^{-(14-pH)}] \times 0.01/10 \quad (1)$$

PANI chains can be thought of as a sequence of C_6H_5NH monounits, as was previously described. One may determine the C_6H_5NH monounit's molar number via

$$n(C_6H_5NH\ monounits)\ (mol) = (PANI)/Mr(unit) \quad (2)$$

The rate of the -NH- protonated by H^+ (R) per cm^2 can be calculated via

$$R = [n(H^+) \times Mr(unit)]/m(PANI) \quad (3)$$

where Mr(unit) is the PANI monounit's relative molecular mass (Mr(unit) = 91.4679).

$M + H^+_{ads} + e \longrightarrow M + H_2$ (4) may be used to get $n(H^+)$, and m(PANI) is the PANI loading mass (g) per cm^2.

2.7 Determination of the turnover frequency (TOF).

The active sites were quantified by CV from -0.2 V to 0.6 V vs. RHE in *pH* 7 phosphate buffer at a scan rate of 50 mV s^{-1}. After determining the quantity of electric charges (Q is the integral of the CV curve), the number of active sites (n) of the catalyst was calculated by the formula n = Q/2F, where F is the Faraday constant (96485 C mol^{-1}). Meanwhile, the TOF plot is calculated from the formula TOF = j/(2Fn)

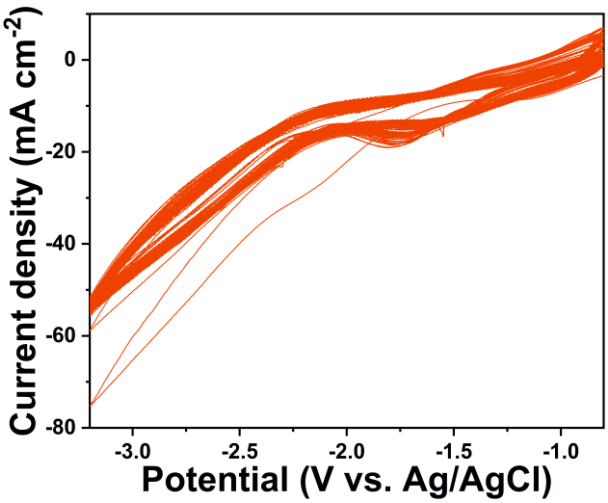

Fig. S1 Cyclic voltammograms of the CF electrode in acetonitrile solution containing p-iodonitrobenzene (6 mM) and tetrabutylammonium hexafluorophosphate (0.15 M): 1_{st} to 210_{th} cycles. Scan rate: 100 mV s^{-1}.

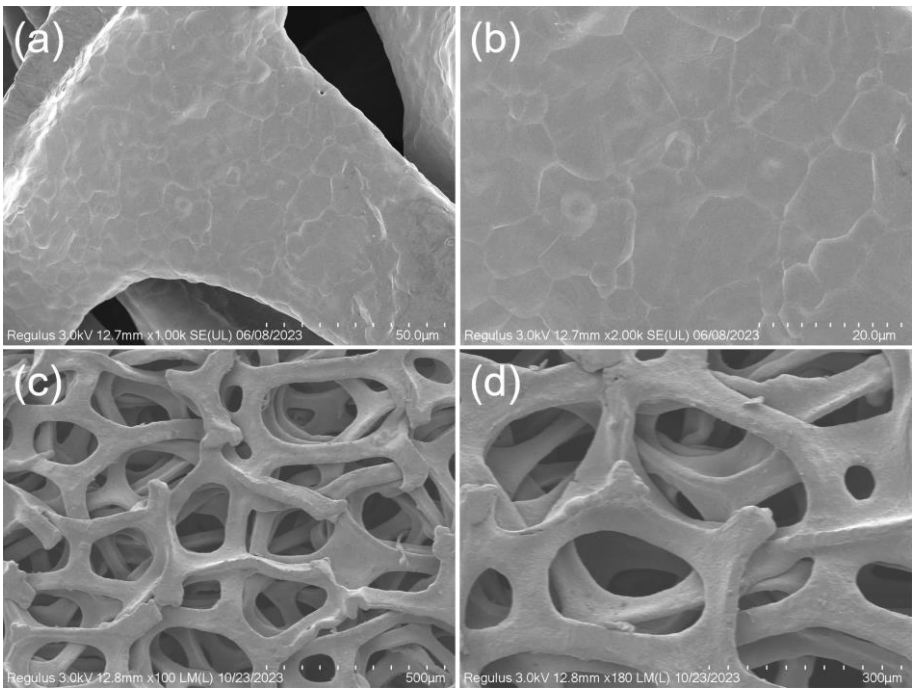

Fig. S2 SEM images of CF in (a) 50 µm, (b) 20 µm, (c) 500 µm, and (d) 300 µm.

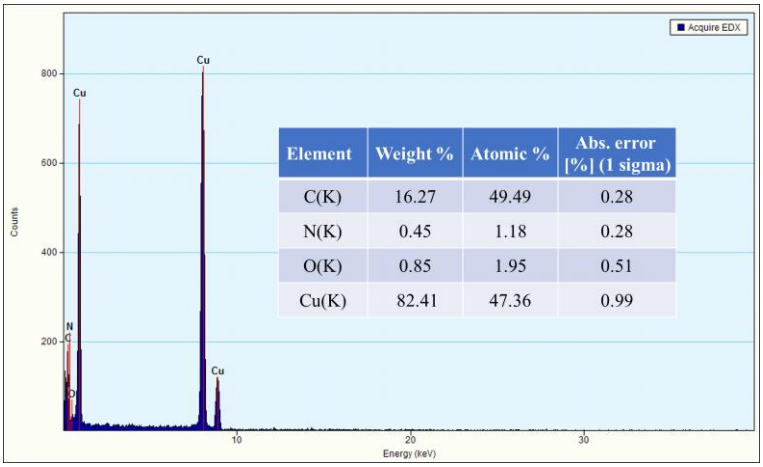

Element	Weight %	Atomic %	Abs. error [%] (1 sigma)
C(K)	16.27	49.49	0.28
N(K)	0.45	1.18	0.28
O(K)	0.85	1.95	0.51
Cu(K)	82.41	47.36	0.99

Fig. S3 EDX spectra and elemental contents of PANI/CF-210.

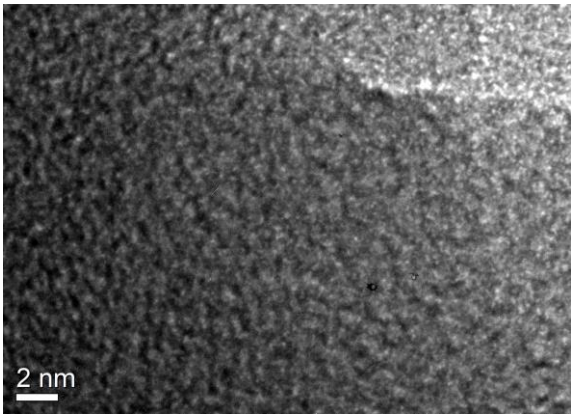

Fig. S4 HRTEM images of PANI/CF-210.

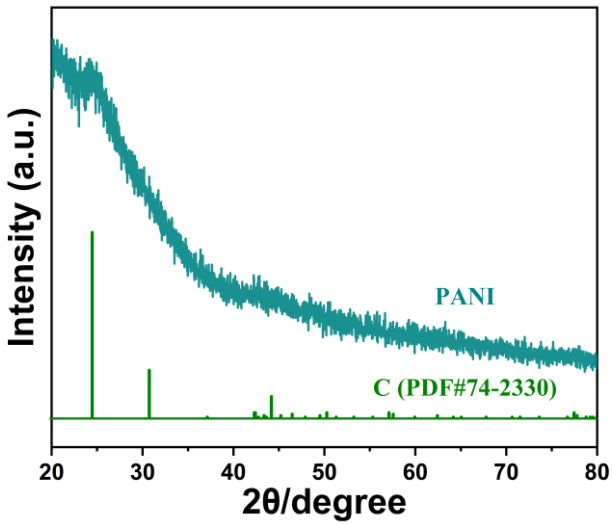

Fig. S5 XRD pattern of bare PANI.

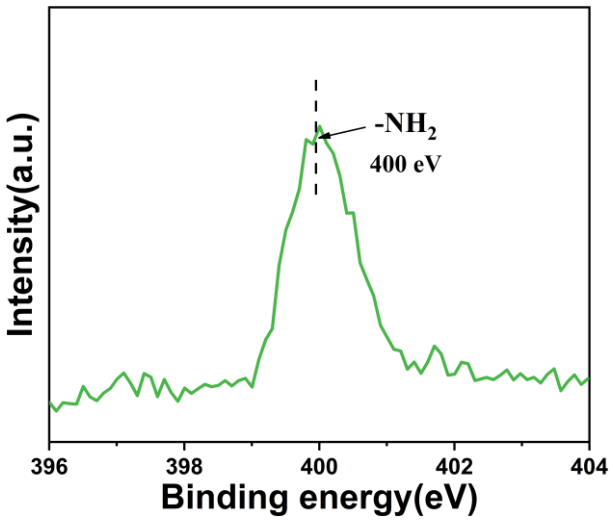

Fig. S6 XPS spectra of N 1s of ANI/CF.

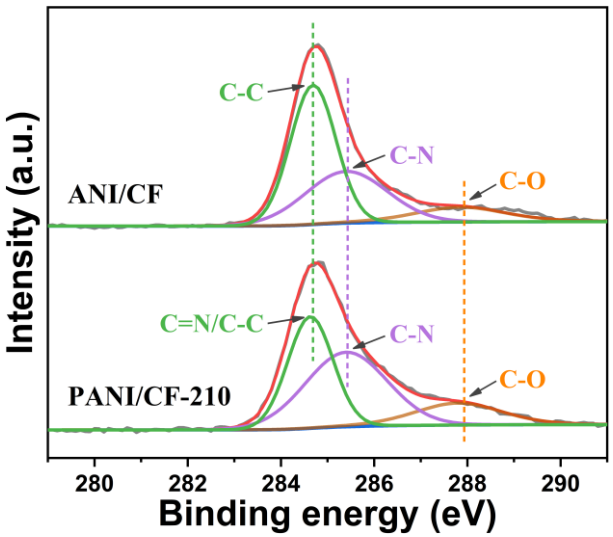

Fig. S7 XPS spectra of C 1s derived from ANI/CF and PANI/CF-210.

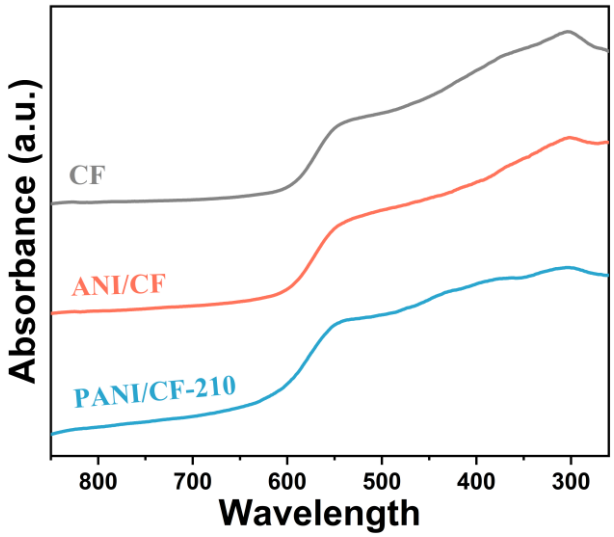

Fig. S8 UV-vis absorption spectra of CF, ANI/CF, and PANI/CF-210.

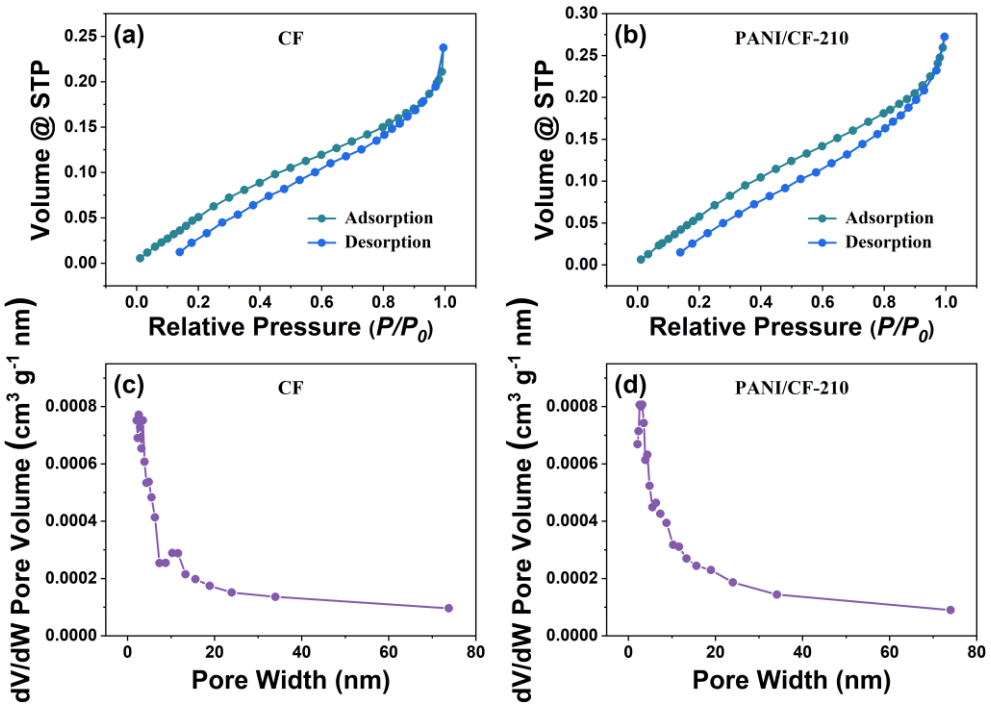

Fig. S9 Nitrogen adsorption/desorption isotherms of (a) CF and (b) PANI/CF-210.

BJH pore size distributions of (c) CF and (d) PANI/CF-210.

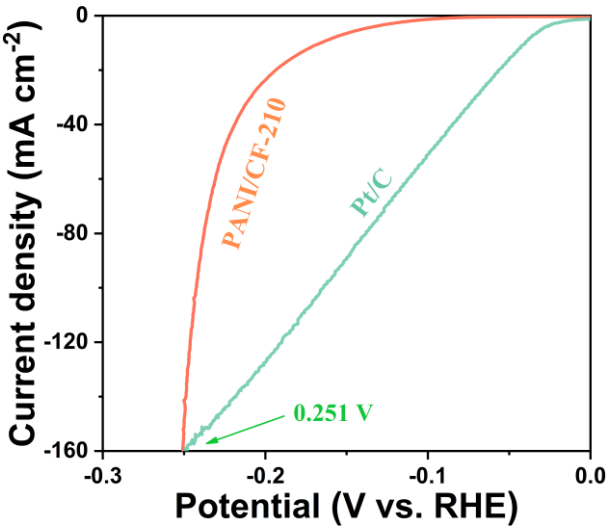

Fig. S10 HER polarization curves of PANI/CF-210 and Pt/C (after iR-correction).

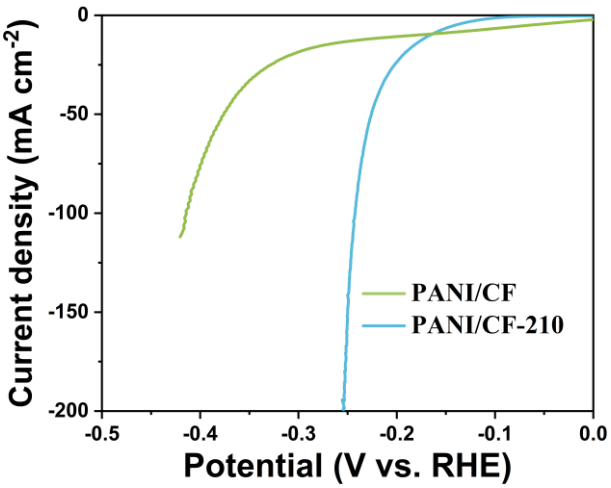

Fig. S11 The comparation of HER polarization curves about PANI modified CF by electrochemical polymerization and electrografting, respectively (after iR-correction).

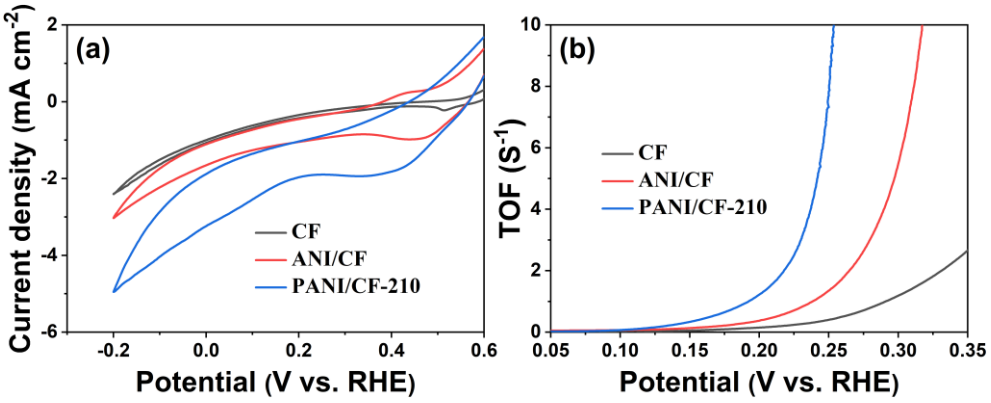

Fig. S12 (a) CVs of CF, ANI/CF, and PANI/CF-210 in *pH* = 7 phosphate buffer between -0.2 V and 0.6 V vs. RHE with a scan rate of 50 mV s^{-1} and their integral area is 0.085, 0.55, 0.97. (b) Turnover frequencies of the CF, ANI/CF, and PANI/CF-210 catalyst in 0.5 M H_2SO_4.

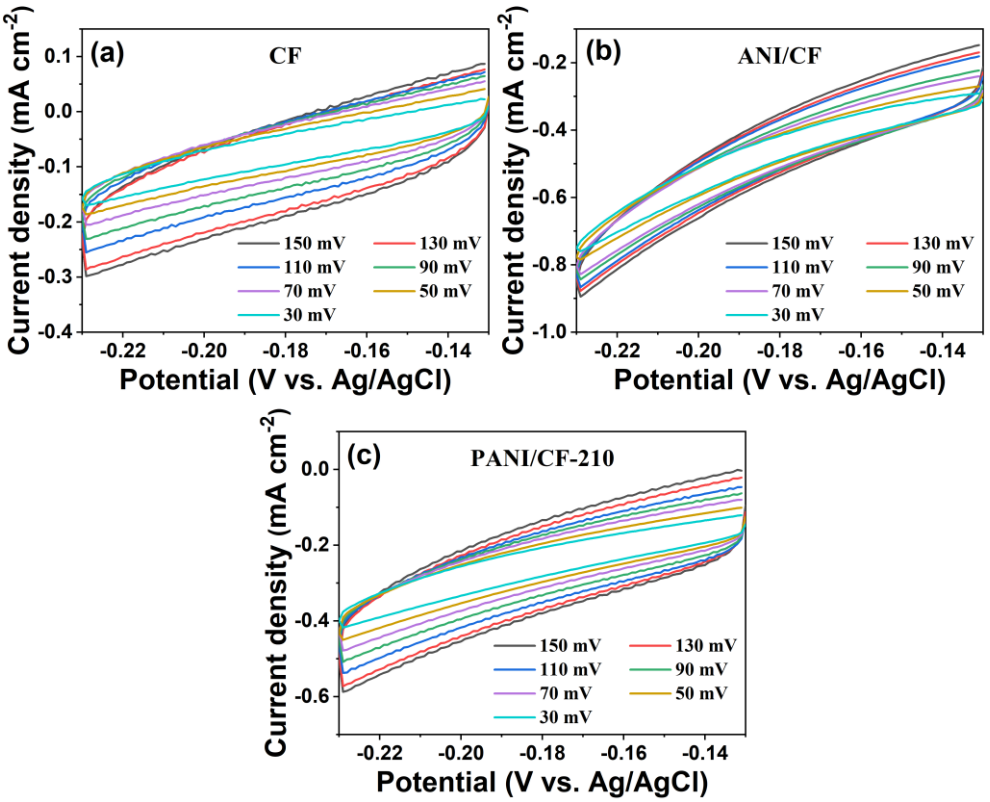

Fig. S13 CV curves of (a) CF, (b) ANI/CF, and (c) PANI/CF-210 at different scan rates, where the curves are taken in a potential window without faradaic processes in a 0.5 M H_2SO_4.

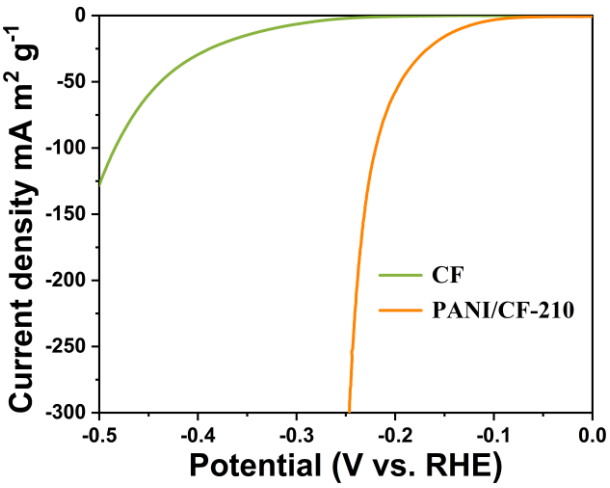

Fig. S14 HER polarization curve of the surface area of the catalyst in relation to the catalytic activity.

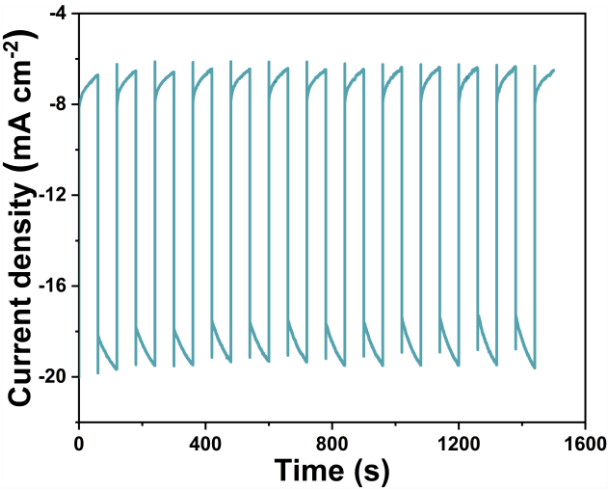

Fig. S15 Multi-voltage process of PANI/CF-210.

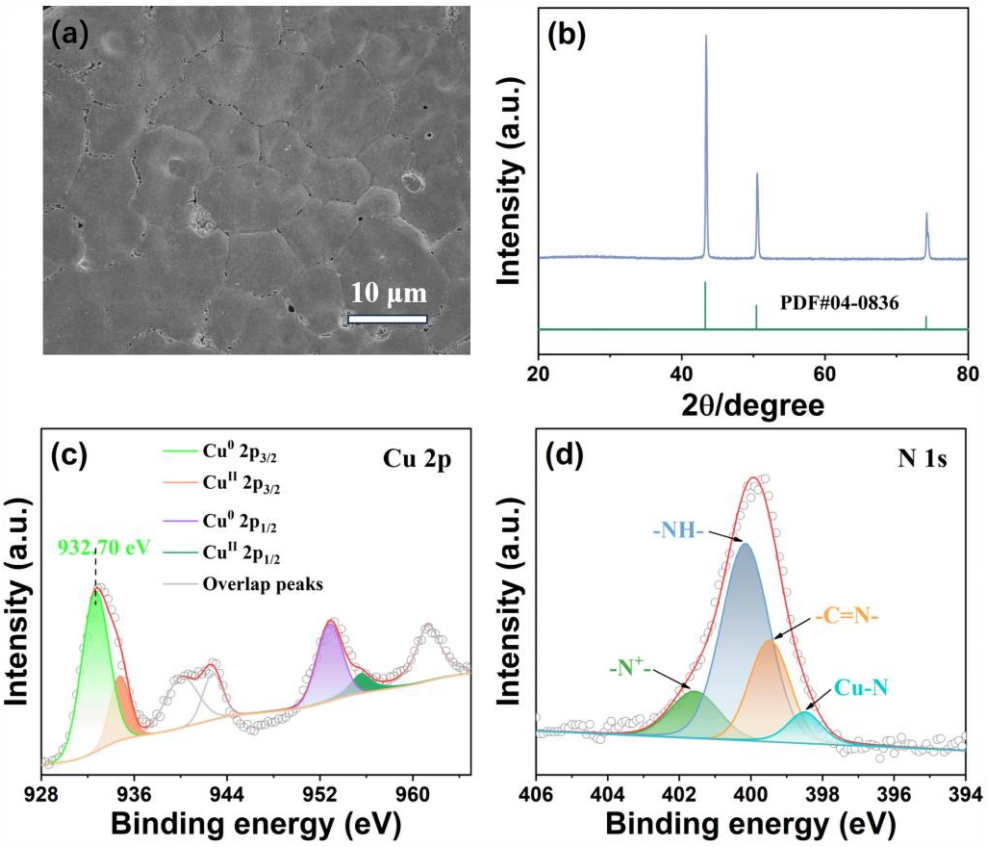

Fig. S16 Morphology and structure characterization after electrolysis in 0.5 M H_2SO_4 for 30 h. (a) SEM images of PANI/CF-210 at 10 μm. (b) XRD patterns of PANI/CF-210 samples. (c) Cu 2p and (d) N 1s XPS spectrum of PANI/CF-210 samples.

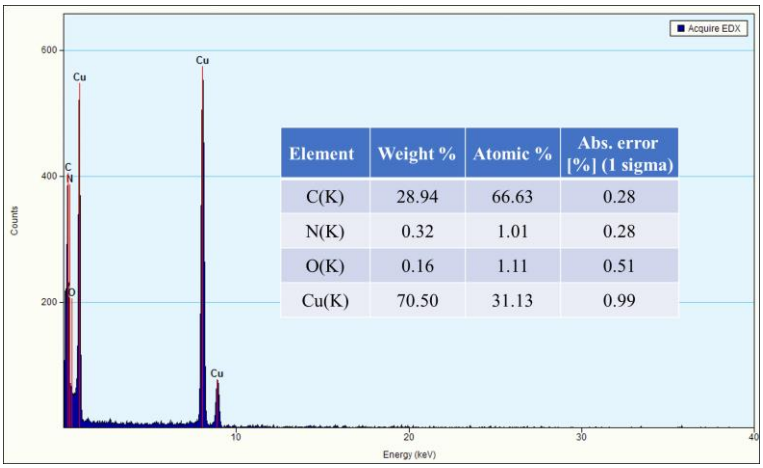

Element	Weight %	Atomic %	Abs. error [%] (1 sigma)
C(K)	28.94	66.63	0.28
N(K)	0.32	1.01	0.28
O(K)	0.16	1.11	0.51
Cu(K)	70.50	31.13	0.99

Fig. S17 EDX spectra and elemental contents of PANI/CF-210 after electrolysis in 0.5 M H_2SO_4 for 30 h.

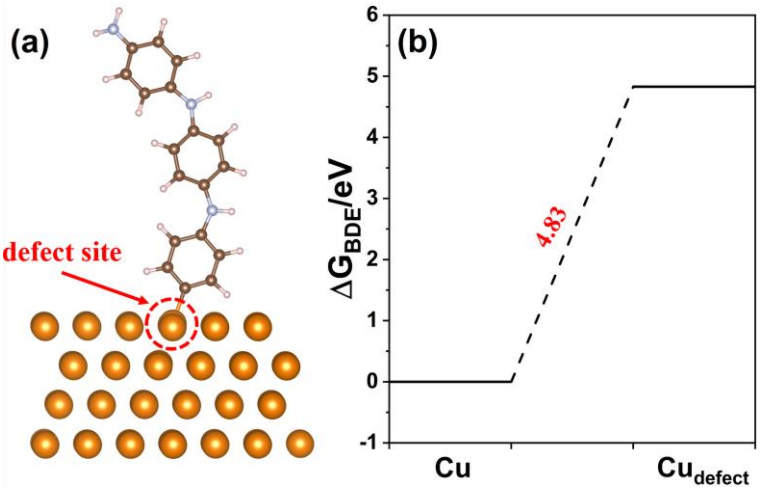

Fig. S18 (a) Theoretical models of the PANI/CF defect site. (b) The change of Gibbs energies during dissociation reaction on PANI-modified Cu(111) surface.

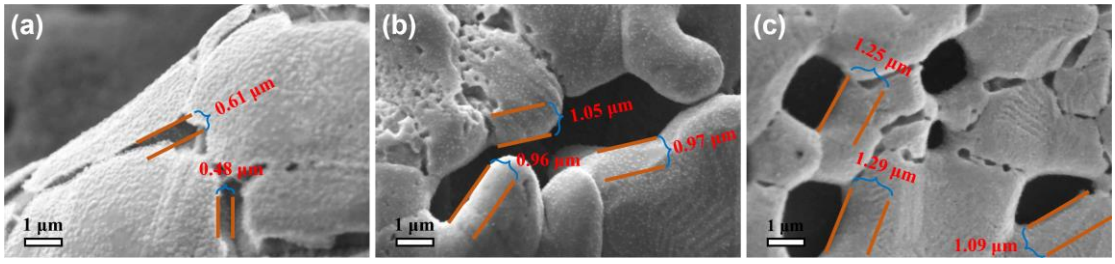

Fig. S19 sectional SEM images of (a) PANI/CF-60, (b) PANI/CF-210, and (c) PANI/CF-300 film.

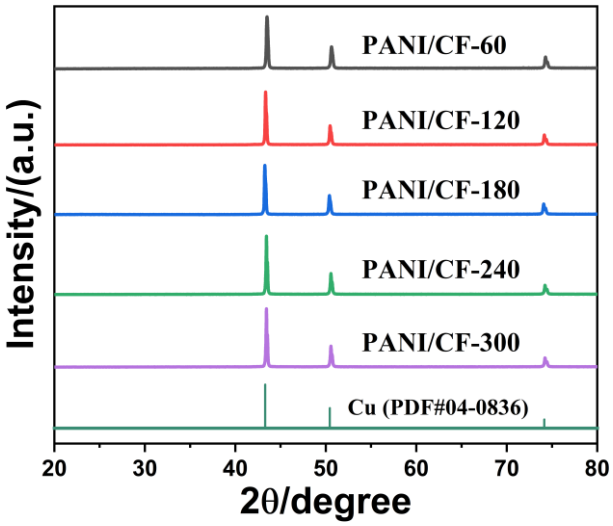

Fig. S20 XRD of CF modified with different thicknesses of organic polymer films.

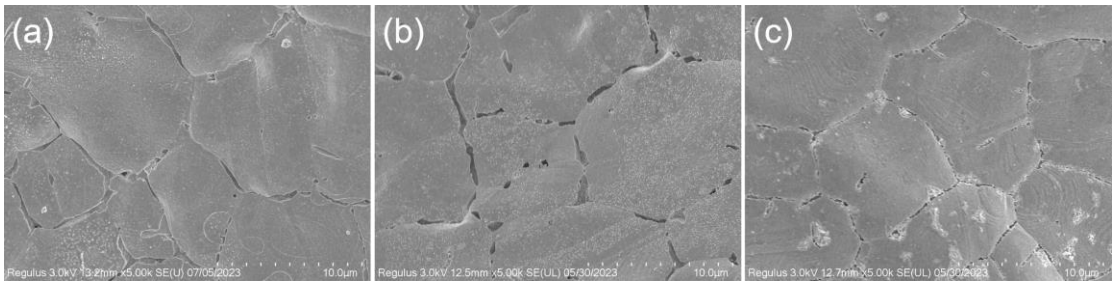

Fig. S21 SEM images of (a) BP/CF-210, (b) m-PANI/CF-210, and (c) o-PANI/CF-210 at 10 μm.

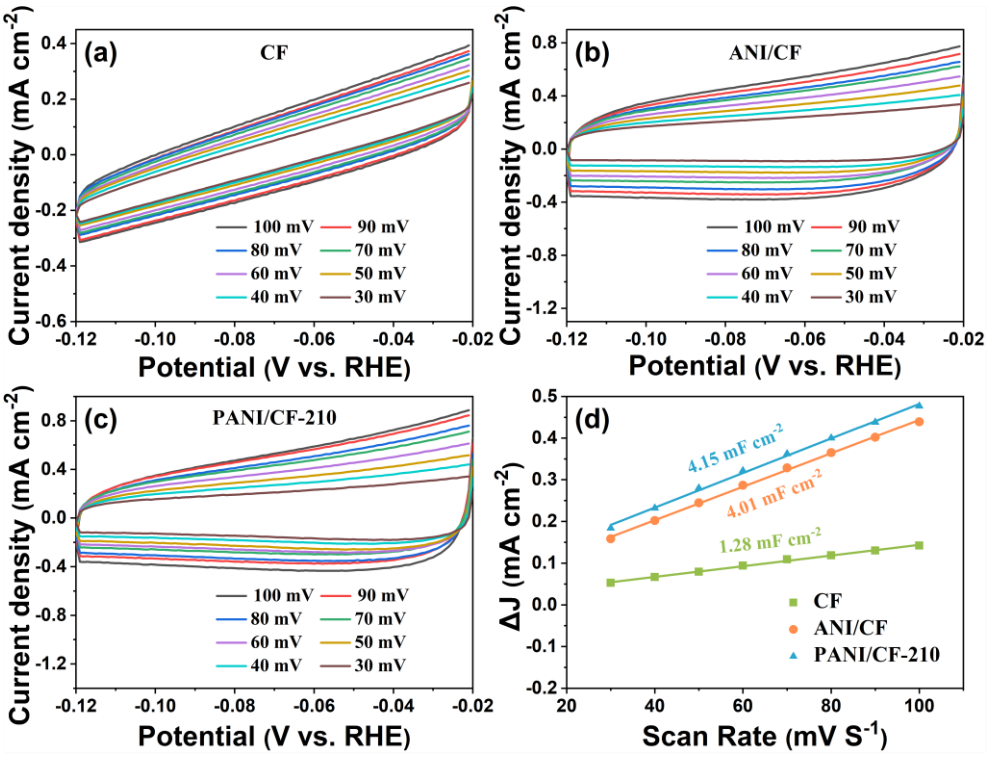

Fig. S22 CV curves of (a) CF, (b) ANI/CF, and (c) PANI/CF-210 at different scan rates, where the curves are taken in a potential window without faradaic processes in a 1.0 M KOH with 1.0 M ethanol. (d) current density as a function of the scanning rates.

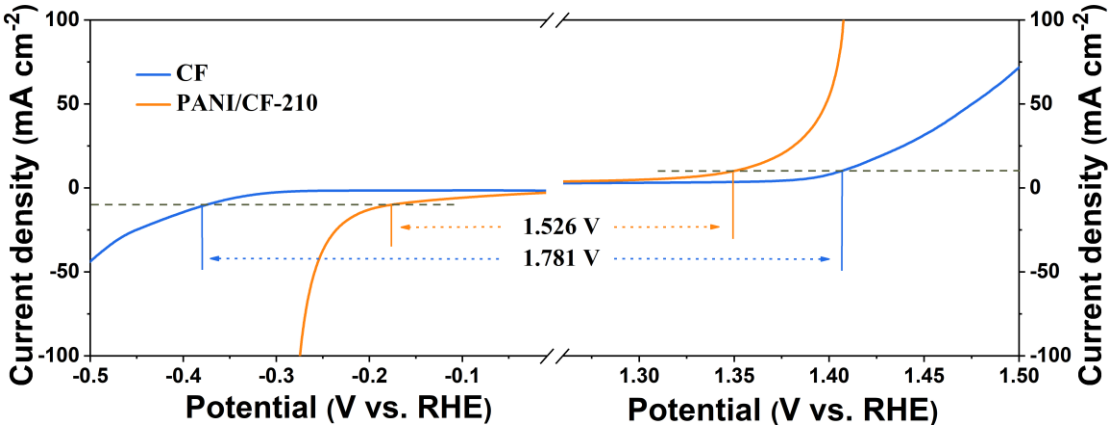

Fig. S23 Total performance diagram of electrodes toward HER and EOR in 1.0 M KOH electrolyte with 1.0 M ethanol.

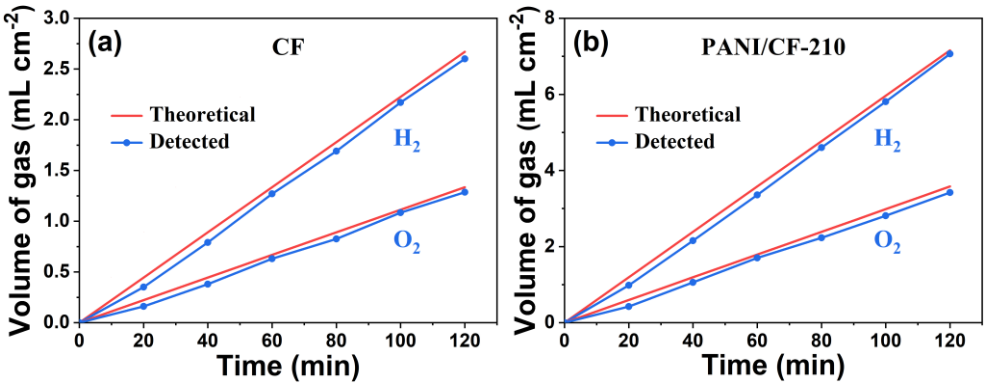

Fig. S24 Theoretical and actual hydrogen and oxygen production of (a) CF (b) PANI/CF-210 at a 200 mV overpotential in 0.5 M H_2SO_4.

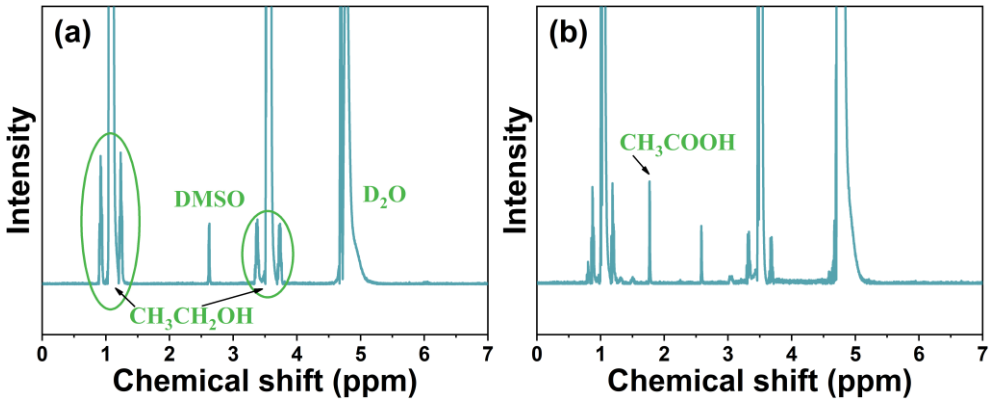

Fig. S25 (a) ^{1}H NMR spectra of PANI/CF-210 before electrolysis in 1.0 M KOH electrolyte with 1.0 M ethanol. (b) ^{1}H NMR spectra of PANI/CF-210 after electrolysis in 1.0 M KOH electrolyte with 1.0 M ethanol.

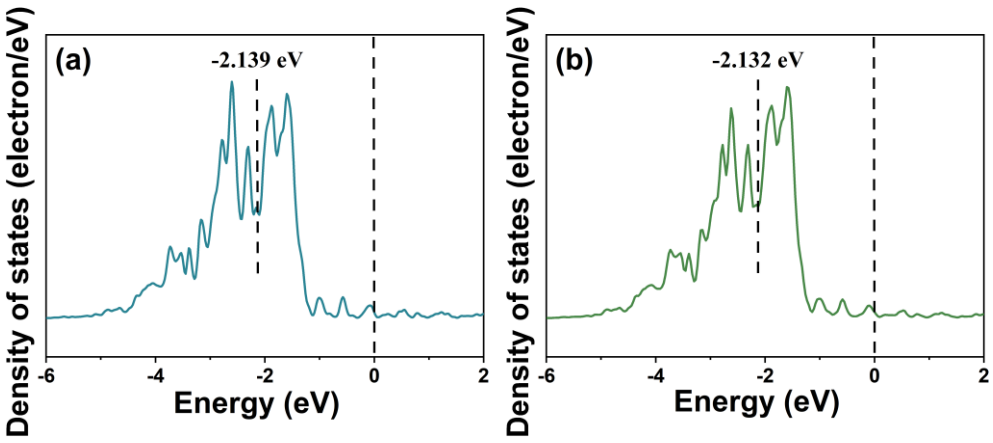

Fig. S26 The calculated d-band center for (a) CF and (b) PANI/CF.

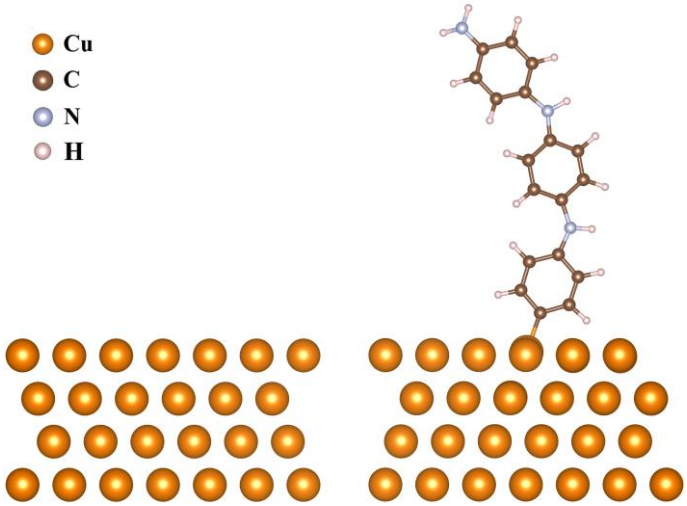

Fig. S27 Theoretical models of the Cu and PANI/CF before hydrogen adsorption.

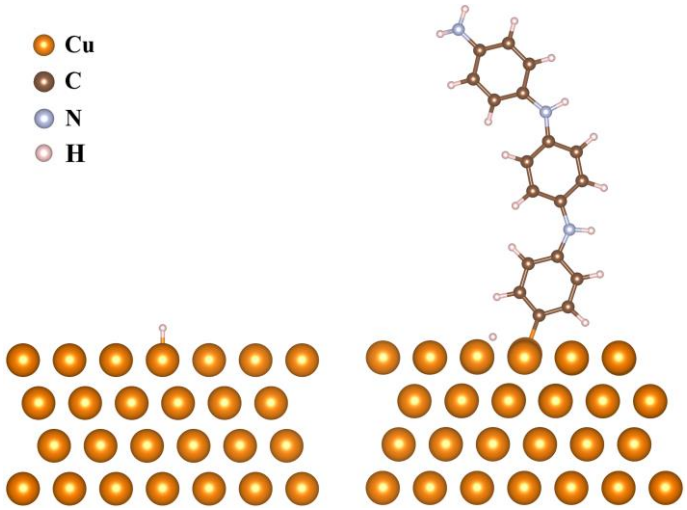

Fig. S28 Theoretical models of the Cu and PANI/CF after hydrogen adsorption.

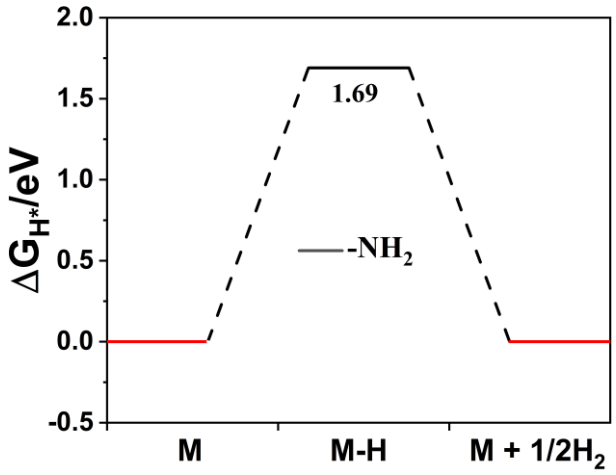

Fig. S29 DFT calculation. The change of Gibbs energies during the HER reaction on PANI-modified Cu(111) surface with -NH_2 as the active center.

Table S1 EIS fitting data of CF, ANI/CF, PANI/CF-210.

Catalyst	R_s (Ω)	R_{ct} (Ω)	CPE ($mS.s^{(1-a)}$)	a
CF	1.70 ± 0.019	65.24 ± 0.92	0.78 ± 0.027	0.80 ± 0.0056
ANI/CF	1.28 ± 0.023	33.62 ± 0.77	1.35 ± 0.092	0.76 ± 0.011
PANI/CF-210	1.21 ± 0.017	11.54 ± 0.16	1.50 ± 0.11	0.74 ± 0.011

Table S2 The comparison of the performance of HER on PANI/CF-210 with some similar electrocatalysts.

Catalyst	Electrolyte	η_{10} (mV)	Ref
PANI/CF-210	0.5 M H_2SO_4	165	This work
PANI/CF-210	1 M KOH	176	This work
Cu-por-py	1 M KOH	250	[1]
Mn_2O_3CuO–VOP	1 M KOH	220	[2]
P1T	0.5 M H_2SO_4	350	[3]
NiMOF−MoS_2	0.5 M H_2SO_4	469	[4]
MnFeCu/g-C_3N_4 NFs	0.5 M H_2SO_4	400	[5]
CeO_2@Cu NRAs	1 M KOH	180	[6]
Cu[Ni(2,3-pyrazinedithiolate)$_2$]	H_2SO_4 (PH=1.3)	330	[7]
Cu_2Se@NiFe-LDHNS	1 M KOH	195	[8]
Ni/Cu-60	0.5 M H_2SO_4	275	[9]
CoCuNiP NSs/3D NF	2 M NaOH	185	[10]
$Cu_{50}Co_{50}P$	1 M KOH	184	[11]

PS-Cu	0.5 M H_2SO_4	182	[12]
$Ni_{85}Cu_{15}$-C	1 M KOH	319	[13]
Cu_1Pd_3-C	1 M KOH	315	[14]
CuU_{90}-E_{20}	1 M KOH	353	[15]
$CuCo_2S_4$/CC	1 M KOH	171	[16]
Cu-NbC	1 M KOH	271	[17]
E-Cu	0.5 M H_2SO_4	180	[18]
B-CoNiOOH/PANI@TiO_2/Ti	1 M KOH	196	[19]
Cu_2CoSnS_4	0.5 M H_2SO_4	233	[20]
Cu_3N@CoNiCHs@CF	1 M KOH	182	[21]
Zn-Co_9S_8@CF-(1-1)	0.5 M H_2SO_4	278	[22]
CeO_2@Cu NRAs	1 M KOH	180	[23]

Table S3 The comparison of the performance of HER on PANI/CF-210 with precious metal electrocatalysts.

Catalyst	Electrolyte	η_{10} (mV)	Ref
PANI/CF-210	0.5 M H_2SO_4	165	This work
PANI/CF-210	1 M KOH	176	This work
Pt/MoS_2/MoO_2/Mo_6S_8	0.5 M H_2SO_4	124	[24]
Pt_{SA}-MIL100(Fe)	0.5 M H_2SO_4	60	[25]
Pt-N@NPC-800	1 M KOH	61	[26]
Pt-Ni@NiMoN	2 M NaCl	11	[27]

Ru_{SA}@NiFe PPc	0.5 M H_2SO_4	12	[28]
Pd(20nm)/SnTe	0.5 M H_2SO_4	86	[29]
Pd/$NiFeO_x$	1 M KOH	180	[30]
N-Pd/A-Co(II)	1 M KOH	58	[31]
Pd_1-$CoSe_2$	1 M KOH	80	[32]
Pd-nanodendrites/GNS	1 M KOH	40	[33]
$PdHCu_{11}$	0.5 M H_2SO_4	50	[34]
Pt_{SA}–Ni_3S_2	1 M KOH	33	[35]
$Ag_2B_{12}H_{12}$	0.5 M H_2SO_4	376	[36]
Ag/Mn_3O_4	0.5 M H_2SO_4	177	[37]
RuM@BCN	1 M KOH	24	[38]
Mo-Ru NSAs	1 M KOH	16	[39]
Ru@V-RuO_2/C HMS	0.5 M H_2SO_4	43	[40]
a-Ru@Co-DHC	1 M KOH	40	[41]
Ru/NC	1 M KOH	22	[42]

Table S4 Deposition conditions of organic polymer modified copper foam electrode.

Catalyst	E (V vs. RHE)	Number of CV scan cycles	Deposition time (s)
PANI/CF-60	-0.8~-3.2	60	1440
PANI/CF-120	-0.8~-3.2	120	2880
PANI/CF-180	-0.8~-3.2	180	4320

PANI/CF-210	-0.8~-3.2	210	5040
PANI/CF-240	-0.8~-3.2	240	5760
PANI/CF-300	-0.8~-3.2	300	7200

References

1. S. K. Das, A. Chowdhury, K. Bhunia, A. Ghosh, D. Chakraborty, M. Das, U. Kayal, A. Modak, D. Pradhan and A. Bhaumik, Ni(II) and Cu(II) grafted porphyrin-pyrene based conjugated microporous polymers as bifunctional electrocatalysts for overall water splitting, *Electrochim. Acta*, 2023, **459**, 142553.
2. S. Bhowmick, A. Sarangi, C. T. Moi, S. Chakraborty and M. Qureshi, Diffusion-Mediated Morphological Transformation in Bifunctional Mn_2O_3/CuO–$(VO)_3(PO_4)_2 \cdot 6H_2O$ for Enhanced Electrochemical Water Splitting, *ACS Appl. Mater. Interfaces*, 2022, **14**, 52204-52215.
3. A. S. Goloveshkin, N. D. Lenenko, M. I. Buzin, V. I. Zaikovskii, A. V. Naumkin and A. S. Golub, Organic interlayers boost the activity of MoS_2 toward hydrogen evolution by maintaining high 1T/2H phase ratio, *Int. J. Hydrog. Energy*, 2023, **48**, 10555-10565.
4. J. C. Janardhanan, N. T. Padmanabhan, S. C. Pillai and H. John, Interface Engineering of 2D NiMOF–MoS_2 Hybrids for Electrocatalytic Hydrogen Evolution, *ACS Sustain. Chem. Eng.*, 2023, **11**, 6890-6902.
5. B. Salah, A. Abdelgawad, Q. Lu, A. K. Ipadeola, R. Luque and K. Eid, synergistically interactive MnFeM (M = Cu, Ti, and Co) sites doped porous g-C_3N_4 fiber-like nanostructures for an enhanced green hydrogen production, *Green Chem.*, 2023, **25**, 6032-6040.
6. X. Zhang, J. Yu, H.-J. Shen, L. Zhang, G.-X. Yang, X.-C. Zhou, J.-J. Feng and A.-J. Wang, Reconstituting Cu^0/Cu^+ synergy with heterostructured CeO_2 enabling energy-efficient bipolar hydrogen generation, *Chem. Eng. J.*, 2023, **475**, 146506.

7. K. Chen, D. Ray, M. E. Ziebel, C. A. Gaggioli, L. Gagliardi and S. C. Marinescu, Cu[Ni(2,3-pyrazinedithiolate)$_2$] Metal–Organic Framework for Electrocatalytic Hydrogen Evolution, *ACS Appl. Mater. Interfaces,* 2021, **13**, 34419-34427.
8. H. Qi, P. Zhang, H. Wang, Y. Cui, X. Liu, X. She, Y. Wen and T. Zhan, Cu_2Se nanowires shelled with NiFe layered double hydroxide nanosheets for overall water-splitting, *J. Colloid Interface Sci.,* 2021, **599**, 370-380.
9. Q. Hu, Y. Liu, X. Zheng, J. Zhang, J. Wang, X. Han, Y. Deng and W. Hu, How the surface Cu layer affected the activity of Ni foil for alkaline hydrogen evolution, *Mater. Sci. Technol.,* 2024, **169**, 11-18.
10. B. Nourmohammadi Khiarak, M. Golmohammad, M. M. Shahraki and A. Simchi, Facile synthesis and self-assembling of transition metal phosphide nanosheets to microspheres as a high-performance electrocatalyst for full water splitting, *J. Alloys Compd.*, 2021, **875**, 160049.
11. D. Bandyopadhyay, S. Ghosh, L. Houben, R. Bar-Ziv and M. Bar-Sadan, Full Water Splitting Electrolyzed by Cu–Co Bimetallic Phosphides, *ACS Appl. Energy Mater.*, 2023, **6**, 10987-10995.
12. W.-J. Kang, Y. Feng, Z. Li, W.-Q. Yang, C.-Q. Cheng, Z.-Z. Shi, P.-F. Yin, G.-R. Shen, J. Yang, C.-K. Dong, H. Liu, F.-X. Ye and X.-W. Du, Strain-Activated Copper Catalyst for pH-Universal Hydrogen Evolution Reaction, *Adv. Funct. Mater.*, 2022, **32**, 2112367.
13. M. A. S. Lima, R. A. Raimundo, A. J. M. Araújo, J. F. G. d. A. Oliveira, F. J. A. Loureiro, D. A. Macedo and M. A. Morales, Nickel-Copper-Carbon based electrocatalysts for oxygen

evolution reaction: Sol-gel synthesis using chitosan, *Int. J. Hydrog. Energy*, 2024, **51**, 663-675.

14. Y. Jeong, S. Shankar Naik, Y. Yu, J. Theerthagiri, S. J. Lee, P. L. Show, H. C. Choi and M. Y. Choi, Ligand-free monophasic CuPd alloys endow boosted reaction kinetics toward energy-efficient hydrogen fuel production paired with hydrazine oxidation, *J Mater Sci Technol*, 2023, **143**, 20-29.
15. M.-Y. Cheng, C.-Q. Cheng, Y. Feng, L.-Q. Fu, F.-F. Zhang, T.-T. Yang, Z. Li, Y.-C. Ruan, Z.-W. Yang, K. Lin, H. Liu and X.-W. Du, Self-supporting copper electrode prepared by ultrasonic impact for hydrogen evolution reaction, *J. Alloys Compd.*, 2022, **916**, 165283.
16. S. Sheng, K. Ye, Y. Gao, K. Zhu, J. Yan, G. Wang and D. Cao, Simultaneously boosting hydrogen production and ethanol upgrading using a highly-efficient hollow needle-like copper cobalt sulfide as a bifunctional electrocatalyst, *J. Colloid Interface Sci.*, 2021, **602**, 325-333.
17. W. Ding, L. Sun, Z. Jia, S. Jin, Z. Wang and W. Zhong, Orbital hybridization manipulated by doped Cu+ in NbC for boosting hydrogen evolution, *J. Alloys Compd.*, 2023, **956**, 170374.
18. Z.-Z. Shi, X. Wang, W.-J. Kang, Y.-M. Bai, J. Yang, H. Liu, C.-K. Dong, P.-F. Yin and X.-W. Du, Copper Nanoparticles with Abundant Defects as a pH-Universal Catalyst for Hydrogen Evolution Reaction, *ACS Appl. Energy Mater.*, 2023, **6**, 10012-10019.
19. W. Hao, C. Fu, Y. Wang, K. Yin, H. Yang, R. Yang and Z. Chen, Coupling boron-modulated bimetallic oxyhydroxide with photosensitive polymer enable highly-active and ultra-stable seawater splitting, *J. Energy Chem.*, 2022, **75**, 26-37.

20. K. K. Joshi, P. M. Pataniya, G. R. Bhadu and C. K. Sumesh, Cu2CoSnS4 electrocatalyst embedded paper working electrodes for efficient, stable, pH universal, and large-current-density hydrogen evolution reaction, *Int. J. Hydrog. Energy*, 2024, **49**, 829-842.

21. S.-Q. Liu, M.-R. Gao, S. Liu and J.-L. Luo, Hierarchically assembling cobalt/nickel carbonate hydroxide on copper nitride nanowires for highly efficient water splitting, *Appl. Catal. B*, 2021, **292**, 120148.

22. B. Dong, J.-Y. Xie, N. Wang, W.-K. Gao, Y. Ma, T.-S. Chen, X.-T. Yan, Q.-Z. Li, Y.-L. Zhou and Y.-M. Chai, Zinc ion induced three-dimensional Co_9S_8 nano-neuron network for efficient hydrogen evolution, *Renew. Energ.*, 2020, **157**, 415-423.

23. X. Zhang, J. Yu, H.-J. Shen, L. Zhang, G.-X. Yang, X.-C. Zhou, J.-J. Feng and A.-J. Wang, Reconstituting Cu^0/Cu^+ synergy with heterostructured CeO_2 enabling energy-efficient bipolar hydrogen generation, *Chem. Eng. J.*, 2023, **475**, 146506.

24. M. Liu, G. Lv, H. Liu, T. Liu, L. Kong and L. Liao, Pt/Mo chalcogenide composite deriving from Pt-Mo_6S_8 by high temperature shock for enhanced HER performance, *Chin Chem Lett*, 2024, **35**, 108459.

25. J. Zhu, Y. Cen, H. Ma, W. Lian, J. Liu, H. Ou, F. Ouyang, L. Zhang and W. Zhang, Pt single atoms meet metal–organic frameworks to enhance electrocatalytic hydrogen evolution activity, *Nanoscale Horiz.,* 2023, **8**, 1273-1281.

26. Y. Dong, J.-B. Chen, J. Ying, Y.-X. Xiao, G. Tian, M. D. Symes and X.-Y. Yang, Efficient Water Dissociation on Confined Ultrafine Pt via Pyridinic N-Enhanced Heavy d−π Interaction, *Chem. Mater,* 2022, **34**, 8271-8279.

27. H. Hu, Z. Zhang, Y. Zhang, T. Thomas, H. Du, K. Huang, J. P. Attfield and M. Yang, An ultra-low Pt metal nitride electrocatalyst for sustainable seawater hydrogen production, *Energy Environ. Sci.*, 2023, **16**, 4584-4592.

28. Z. Kou, Y. Liu, W. Cui, B. Yang, Z. Li, R. D. Rodriguez, Q. Zhang, C.-L. Dong, X. Sang, L. Lei, T. Zhang and Y. Hou, Electronic structure optimization of metal–phthalocyanine via confining atomic Ru for all-pH hydrogen evolution, *Energy Environ. Sci.*, 2024, DOI: 10.1039/D3EE03896C.

29. Q. Qu, B. Liu, W. S. Lau, D. Pan and I. K. Sou, Highly active hydrogen evolution facilitated by topological surface states on a Pd/SnTe heterostructure, *Cell Rep. Phys. Sci.,* 2023, **4**, 101332.

30. W. Zhang, X. Jiang, Z. Dong, J. Wang, N. Zhang, J. Liu, G.-R. Xu and L. Wang, Porous Pd/NiFeO$_x$ Nanosheets Enhance the pH-Universal Overall Water Splitting, *Adv. Funct. Mater.*, 2021, **31**, 2107181.

31. L. Li, Y. Ji, X. Luo, S. Geng, M. Fang, Y. Pi, Y. Li, X. Huang and Q. Shao, Compressive Strain in N-Doped Palladium/Amorphous-Cobalt (II) Interface Facilitates Alkaline Hydrogen Evolution, *Small*, 2021, **17**, 2103798.

32. X. Zhao, X. Li, D. Xiao, M. Gong, L. An, P. Gao, J. Yang and D. Wang, Isolated Pd atom anchoring endows cobalt diselenides with regulated water-reduction kinetics for alkaline hydrogen evolution, *Appl. Catal. B,* 2021, **295**, 120280.

33. L. Karuppasamy, L. Gurusamy, S. Anandan, C.-H. Liu and J. J. Wu, Graphene nanosheets supported high-defective Pd nanocrystals as an efficient electrocatalyst for hydrogen evolution reaction, *Chem. Eng. J.,* 2021, **425**, 131526.

34. R. P. Brocha Silalahi, Y. Jo, J.-H. Liao, T.-H. Chiu, E. Park, W. Choi, H. Liang, S. Kahlal, J.-Y. Saillard, D. Lee and C. W. Liu, Hydride-containing 2-Electron Pd/Cu Superatoms as Catalysts for Efficient Electrochemical Hydrogen Evolution, *Angew. Chem. Int. Ed.,* 2023, **62**, e202301272.

35. K. L. Zhou, C. B. Han, Z. Wang, X. Ke, C. Wang, Y. Jin, Q. Zhang, J. Liu, H. Wang and H. Yan, Atomically Dispersed Platinum Modulated by Sulfide as an Efficient Electrocatalyst for Hydrogen Evolution Reaction, *Sci. Adv.*, 2021, **8**, 2100347.

36. M. H. Khan, C. Han, X. Wang, W. Li, G. Zhang and Z. Huang, Synthesis of Silver Nanoparticles from Silver Closo-Dodecaborate Film for Enhanced Hydrogen Evolution, *Small*, 2023, 2305117.

37. R. Cheng, K. Li, H. Li, F. Sun, X. He, T. Zhao, J. Zhang and C. Fu, In-situ transformed Mott–Schottky heterointerface in silver/manganese oxide nanorods boosting oxygen reduction, oxygen evolution, and hydrogen evolution reactions, *Nano Res.,* 2023, DOI: 10.1007/s12274-023-6240-7.

38. T. Qiu, J. Cheng, Z. Liang, H. Tabassum, J. Shi, Y. Tang, W. Guo, L. Zheng, S. Gao, S. Xu and R. Zou, Unveiling the nanoalloying modulation on hydrogen evolution activity of ruthenium-based electrocatalysts encapsulated by B/N co-doped graphitic nanotubes, *Appl. Catal. B*, 2022, **316**, 121626.

39. L. Li, S. Liu, C. Zhan, Y. Wen, Z. Sun, J. Han, T.-S. Chan, Q. Zhang, Z. Hu and X. Huang, Surface and lattice engineered ruthenium superstructures towards high-performance bifunctional hydrogen catalysis, *Energy Environ. Sci.*, 2023, **16**, 157-166.

40. Y. Li, W. Wang, M. Cheng, Y. Feng, X. Han, Q. Qian, Y. Zhu and G. Zhang, Arming Ru with Oxygen-Vacancy-Enriched RuO_2 Sub-Nanometer Skin Activates Superior Bifunctionality for pH-Universal Overall Water Splitting, *Adv. Mater.*, 2023, **35**, 2206351.
41. W. Yang, W. Zhang, R. Liu, F. Lv, Y. Chao, Z. Wang and S. Guo, Amorphous Ru nanoclusters onto Co-doped 1D carbon nanocages enables efficient hydrogen evolution catalysis, *Chinese J. Catal.*, 2022, **43**, 110-115.
42. S. Zhu, Z. Li, L. Hou, M. G. Kim, H. Jang, S. Liu and X. Liu, Revealing the Role of Electronic Asymmetricity on Supported Ru Nanoclusters for Alkaline Hydrogen Evolution Reaction, *Adv. Funct. Mater.*, 2023, 2314899.